

Cloud-Top Properties of Growing Cumulus prior to Convective Initiation as Measured by Meteosat Second Generation. Part II: Use of Visible Reflectance

JOHN R. MECIKALSKI AND WAYNE M. MACKENZIE JR.

Earth Systems Science Center, University of Alabama in Huntsville, Huntsville, Alabama

MARIANNE KÖNIG

European Organisation for the Exploitation of Meteorological Satellites (EUMETSAT), Darmstadt, Germany

SAM MULLER

Jupiter's Call, LLC, Madison, Alabama

(Manuscript received 22 January 2010, in final form 12 August 2010)

ABSTRACT

This study is a companion research effort to “Part I,” which emphasized use of infrared data for understanding various aspects of growing convective clouds in the Meteosat Second Generation (MSG) satellite’s Spinning Enhanced Visible and Infrared Imager (SEVIRI) imagery. Reflectance and derived brightness variability (BV) fields from MSG SEVIRI are used here to understand relationships between cloud-top signatures and physical processes for growing cumulus clouds prior to known convective initiation (CI) events, or the first occurrence of a ≥ 35 -dBZ echo from a new convective cloud. This study uses daytime SEVIRI visible (VIS) and near-infrared (NIR) reflectances from 0.6 to 3.9 μm (3-km sampling distance), as well as high-resolution visible (1-km sampling distance) fields. Data from 123 CI events observed during the 2007 Convection and Orographically Induced Precipitation Study (COPS) field experiment conducted over southern Germany and northeastern France are processed, per convective cell, so to meet this study’s objectives. These data are those used in Part I. A total of 27 VIS–NIR and BV “interest fields” are initially assessed for growing cumulus clouds, with correlation and principal component analyses used to highlight the fields that contain the most unique information for describing principally cloud-top glaciation, as well as the presence of vigorous updrafts. Time changes in 1.6- and 3.9- μm reflectances, as well as BV in advance of CI, are shown to contain the most unique information related to the formation and increase in size of ice hydrometeors. Several methods are proposed on how results from this analysis may be used to monitor growing convective clouds per MSG pixel or per cumulus cloud “object” over 1-h time frames.

1. Introduction

This paper is a companion to a study that uses infrared (IR) fields from the Spinning Enhanced Visible and Infrared Imager (SEVIRI) aboard the Meteosat Second Generation (MSG) meteorological satellite to evaluate growing cumulus clouds 30–60 min prior to convective initiation (CI; Mecikalski et al. 2010, hereinafter Part I). As in Part I, this study is *not* focused on nowcasting (0–1-h

forecasting); rather, the purpose is to gain insights into how the array of SEVIRI visible (VIS) and near-infrared (NIR) fields may be used to understand and monitor growing cumulus clouds in advance of CI. CI, defined here as the first occurrence of a radar echo of ≥ 35 -dBZ intensity at ground level from a convective cloud, is an active area of study (Weckwerth and Parsons 2006) for which satellite analyses offer considerable value. Geostationary satellites view growing clouds before a radar echo is observed, by ~ 1 h in some cases (Roberts and Rutledge 2003).

SEVIRI offers opportunities to evaluate how four VIS–NIR channels of information, plus 1-km high-resolution VIS (HRV) brightness data, can be used for these purposes.

Corresponding author address: John R. Mecikalski, Dept. of Atmospheric Science, University of Alabama in Huntsville, NSSTC, 320 Sparkman Dr., Huntsville, AL 35805-1912.
E-mail: john.mecikalski@nsstc.uah.edu

The 0.6-, 0.8-, 1.6-, and 3.9- μm channels provide reflectance information, with the 3.9- μm channel requiring processing in order to separate the emitted and reflected components in the radiance data. Therefore, this study extends Part I by enhancing the daytime ability to evaluate several cumulus cloud attributes. In Part I, the physical attributes determined via IR data processing are 1) in-cloud updraft strength (an inferred physical *process*); 2) cumulus cloud width (i.e., updraft width), and the process of feature expansion; 3) cloud depth, or the height of the updraft; and 4) cloud-top glaciation (and inferred microphysical processes). Reflectance fields as used in this study will be especially helpful in evaluating the fourth attribute, cloud-top glaciation, given that NIR reflectance (i.e., 1.6 and 3.9 μm) decreases once cloud tops transition from liquid water droplets to ice hydrometeors (Baum et al. 2000a; Setvák et al. 2003; Lindsey et al. 2006). These data can also infer optical depth via the 0.6- and 0.8- μm channels (Greenwald and Christopher 2000), particle size from the 1.6- μm channel (Levizzani and Setvák 1996), and updraft strength estimates from the 3.9- μm reflectance as related to changing mean size (effective radius) distributions of cloud-top ice particles (Setvák et al. 2003) over time as clouds grow.

The goals of this study are therefore 1) to extend our understanding on how various sources of information from VIS–NIR channels may be used to monitor physical attributes and inferred processes within new cumulus clouds, relating VIS–NIR cloud-top observations to aspects of cumulus clouds prior to CI, and 2) to evaluate the most useful subset of channels and derived fields (from the four SEVIRI solar channels, along with HRV information) that best describe the important aspects of developing cumuli. Once known, specific SEVIRI fields will be defined for use in convective cloud monitoring. However, as in Part I, because of the above goals and how the study was conducted via the human-expert analysis of CI events, *this paper will not cover aspects of validation and skill score analysis of a specific nowcasting algorithm*; these topics are subjects of future studies.

Section 2 provides a background on previous research related to how solar reflectance (VIS–NIR) data from geostationary satellites have been used to interpret and monitor developing cumulus clouds, and hence the motivation for this type of research. Section 3 provides an overview of the MSG datasets used and how they were processed. In section 3, the information specific to the 2007 Convection and Orographically Induced Precipitation Study (COPS) field experiment is provided, as it was over this region (southern Germany and northeastern France) where CI events were identified and MSG data were analyzed. Section 4 presents the results. The main conclusions are discussed and the paper is concluded in section 5.

2. Background

Visible imagery is that within the 0.4–0.7- μm range, with components of reflected solar radiation being seen in wavelengths below $\sim 4 \mu\text{m}$, and has been used to interpret and monitor convective clouds beginning with the Gemini and Apollo space missions of the 1960s. Visible satellite data analysis expanded with the launch of the first geostationary satellites, the U.S. Applications Technology Series (ATS; 1966–74), for routine observations. This was followed by the Synchronous Meteorological Satellite (SMS), with the Geostationary Operational Environmental Satellite (GOES) launched in 1975. Studies by Purdom (1976, 1982) describe early uses of VIS imagery from ATS and GOES, respectively, for understanding mesoscale and convective-scale cloud patterns in relationship to phenomena that had previously only been described by radar and surface observations. As the resolution of the *GOES-1* VIS ($\sim 0.65 \mu\text{m}$) channel reached 2 km, and finally 1 km with *GOES-2* and beyond, detailed analyses of thunderstorm outflows, sea-breeze patterns in cumulus clouds, and thunderstorm initiation could be made (Purdom 1976, 1982; Weiss and Purdom 1974, Gurka 1986). Adler and Mack (1986) present analysis on how the 1-km VIS channel on GOES may be used to understand cumulus and cumulonimbus cloud-top dynamics. By the late 1970s through the mid-1980s, VIS data became available from other satellites across the globe; in particular the Japanese Geostationary Meteorological Satellite (GMS) and the European Meteorological Satellite (Meteosat) series. Kidder and Vonder Haar (1995, chapters 4 and 9) provide a sound overview of techniques that exploit VIS data for applications related to weather analysis and precipitation estimation.

Polar-orbiting satellites like the Advanced Very High Resolution Radiometer (AVHRR) and the Defense Meteorological Satellite Program (DMSP) instruments allowed for cloud detection and analyses using the VIS channel as well (Isaacs and Barnes 1987; Ebert 1987; Heidinger, et al. 2004), with Landsat (Wielicki and Welch 1986) and Visible Infrared Imager Radiometer Suite (VIIRS; Hutchison et al. 2005) data being used in a similar manner. Present instruments such as the Moderate Resolution Infrared Spectroradiometer (MODIS) possess several channels within the VIS–NIR spectrum, which are used for cloud typing (see Baum et al. 1997, 2000a,b).

As our motivation is to understand how 1–3-km sampling distance VIS–NIR data alone may be used to infer attributes of growing convective clouds, it is important to understand what physical processes may be understood by viewing cumulus clouds with these data. As noted above, the main contributions come in three forms: 1) reflectance, and its time rate of change; 2) visual or automated methods

to detect and measure feature expansion; and 3) scene brightness variability (BV), and its time rate of change.

Solar reflectance and reflectance changes help us to glean information on cloud-top microphysical composition and optical depth. Scorer (1986) describes the characteristics of channel 3 ($3.7 \mu\text{m}$) on the AVHRR instruments, representing cloud-top appearances as a complex dependency on both the thermal and reflected components this channel contains. The thermal and reflected components are functions of temperature, emissivity, transparency, and an asymmetry parameter that parameterizes the scattering characteristics of the cloud and/or ground, while the $3.7\text{--}3.9\text{-}\mu\text{m}$ reflected component is also a function of solar zenith angle. Therefore, channel 3 on AVHRR has been used in the detection of ice particles, or a changeover from water to ice as part of the glaciation process. The work of Setvák and Doswell (1991), furthered by Lindsey et al. (2006), represents the method for retrieving the reflected component of the MSG or GOES $3.9\text{-}\mu\text{m}$ channel and subsequently how small-scale ($\sim(1\text{--}2 \text{ km})$) variability in reflectance relates to cloud-top microphysics and in-cloud dynamics and updraft strength. Setvák et al. (2003), Rosenfeld et al. (2008), and Lensky and Rosenfeld (2008) have demonstrated how $3.9\text{-}\mu\text{m}$ data may be used to evaluate convective storm intensity on a per storm basis, maximizing the use of the reflectance information as a means of estimating cloud-top microphysics (Hunt 1973), specifically the effective radii of frozen hydrometeors and relating this back to updraft intensity. In essence, strong updrafts result in rapid freezing at temperatures below -30°C before substantial hydrometeor growth, and mostly small-sized ice crystals (Rosenfeld et al. 2008).

The texture or variability in the brightness of a scene, especially in high-resolution data ($\leq 1 \text{ km}$), can allow for the evaluation of two aspects of the preconvective environment. First, in cases where CI occurs due to surface heating in atmospheres not obscured by middle- or high-level clouds, fields of cumulus clouds will produce large variability in the brightness of a $\leq 1\text{-km}$ resolution image. Specifically, spatial variability is produced by bright cumulus cloud pixels immediately adjacent to clear-sky pixels of Earth's surface. Second, with very high-resolution data ($< 100 \text{ m}$), the physical aspects of individual turrets or overshoots of growing updrafts-cumulus can be estimated. With MSG HRV data being 1 km , we are able to evaluate the gross aspects of texture, more so representing the general lumpy character of cumuli tops rather than very detailed features.

Using information from IR data for assessing the physical attributes of growing convective clouds (Part I), the plan is to include HRV and VIS-NIR information as well to enhance the monitoring of growing cumulus

clouds during daytime, when most new thunderstorms form. Within the 0–1-h time frame from the present, linearly extrapolating current trends into the near future is one approach that has shown promise for identifying new CI events, producing forecast lead times of $\sim(10\text{--}45)$ min (Iskenderian et al. 2009). This is done by processing geostationary satellite data that only contain information on developing cumulus clouds. The Satellite Convection Analysis and Tracking system (SATCAST; Mecikalski et al. 2010) nowcasts CI by monitoring individual cumuli, presently using only IR data. As in Part I, sequences of 15-min time-interval MSG images are analyzed to help understand how to properly interpret satellite signatures ahead of thunderstorm development, with the hope that CI nowcasting within 0–1-h time frames may be improved significantly (in terms of nowcast skill).

3. MSG imagery and interest field development

a. Level 1.5 channel data

Part I contains much information relevant to the present study; that pertinent to MSG SEVIRI channels that contain reflectance information is discussed herein. VIS, NIR, and IR data at 3-km sampling distance, with HRV at 1-km sampling distance, are collected by SEVIRI on the MSG (specifically *Meteosat-9*) satellite as located over the equator at 0° longitude. The VIS, NIR, and IR (HRV) resolution is 3 (1) km. Over the COPS region the along-pixel resolution is near 5–7 (2–3) km due to skewing effects, while cross-pixel resolution is near the nadir value. SEVIRI possesses eight IR channels, with the central wavelengths being 3.9, 6.2, 7.3, 8.7, 9.7, 10.8, 12.0, and $13.4 \mu\text{m}$; two NIR (0.8- and $1.6\text{-}\mu\text{m}$ channels); one VIS centered on $0.6 \mu\text{m}$; and the HRV (Schmetz et al. 2002; EUMETSAT 2007). All data used for this project were collected between 0815 and 1900 UTC,¹ daylight hours over the COPS region in summer, early June–early August.

Reflectances at 0.6, 0.8, and $1.6 \mu\text{m}$ ($\text{Refl}_{0.6}$, $\text{Refl}_{0.8}$, and $\text{Refl}_{1.6}$, respectively), as well as HRV brightnesses, are normalized by solar zenith angle (A_{sz}) by $[1/\cos(A_{sz})]$. Here, A_{sz} is a function of latitude, longitude, and time of day. This normalization is done to avoid a diurnal signal in the results. Lindsey et al. (2006) and Rosenfeld et al. (2008) describe a procedure for computing the $3.9\text{-}\mu\text{m}$ reflectance, while Rosenfeld et al. (see also Setvák and Doswell 1991; Lensky and Rosenfeld 2008) present the method specific to MSG. In addition, A_{sz} is required for obtaining the $3.9\text{-}\mu\text{m}$ reflectance which is considered A_{sz} normalized.

¹ Local times are UTC + 30 min for the COPS region.

With cloud transmissivity assumed to be ~ 0 for optically thick clouds, 3.9- μm -specific reflectance ($\text{Refl}_{3.9}$) is found by

$$\text{Refl}_{3.9} = 100 \left[\frac{(R_{\text{total}} - R_{\text{therm}})}{(S - R_{\text{therm}})} \right]. \quad (1)$$

In Eq. (1), R_{total} is the total radiance, R_{therm} is the CO_2 -corrected thermal component of the radiance, and S is the top-of-the-atmosphere solar constant, for the 3.9- μm channel. The units for R_{total} , R_{therm} , and S are $[\text{mW m}^{-2} \text{sr}^{-1} (\text{cm}^{-1})^{-1}]$ ($\text{sr} = \text{steradian}$). Here, $\text{Refl}_{3.9}$ is a percentage, 0–100. The value of R_{therm} is computed (assuming cloud emissivity is 1) as

$$R_{\text{therm}} = R[\text{IR}_{3.9}, T_B(\text{IR}_{10.8})]C_{\text{R}3.9}, \quad (2)$$

where the first term $\{R[\text{IR}_{3.9}, T_B(\text{IR}_{10.8})]\}$ represents the procedure of converting the IR brightness temperature (T_B) of the 10.8- μm channel back to radiance using essentially the Planck function, given as

$$R(v_c) = \frac{C_1 v_c^3}{\exp[C_2 v_c / (AT_B + B)] - 1}. \quad (3)$$

Coefficients A and B are those for SEVIRI's 3.9- μm channel (0.9959 and 3.3592, respectively). Also in Eq. (3), C_1 and C_2 are $1.191\,04 \text{ mW m}^{-2} \text{sr}^{-1} (\text{cm}^{-1})^{-4}$ and $1.438\,77 \text{ K} (\text{cm}^{-1})^{-1}$, respectively, and v_c is the central wavenumber of the channel being processed. In Eq. (2), $C_{\text{R}3.9}$ accounts for the CO_2 absorption as given by

$$C_{\text{R}3.9} = \frac{[T_{\text{B}10.8} - 0.25(T_{\text{B}10.8} - T_{\text{B}13.4})]^4}{(T_{\text{B}10.8})^4}. \quad (4)$$

In Eq. (4) $T_{\text{B}10.8}$ and $T_{\text{B}13.4}$ are the 10.8- and 13.4- μm T_B s, respectively. In Eq. (1), S is found by

$$S = \frac{4.92}{D^2} \cos(A_{\text{sz}}) \exp[-(1 - C_{\text{R}3.9})] \\ \times \exp[-(1 - C_{\text{R}3.9})] \frac{\cos(A_{\text{sz}})}{\cos(A_{\text{sat}})}, \quad (5)$$

where D is the Earth–sun distance and A_{sat} is the satellite zenith angle.

Data at time intervals of 15 min are processed. (Note that although 5-min “rapid scan” data were available during a portion of COPS 2007 from MSG, previous CI research utilizes 15-min time-trend fields, and hence the decision was made to follow past work.) All processing focused on the main updrafts of cumulus clouds, and hence clouds that are considered “optically thick” where the transmission from below is considered negligible, ensured by the choice of the coldest pixel. Beginning with a small 3×3 pixel region centered on growing cumulus

clouds, the coldest IR pixel at 10.8 μm is labeled the main updraft (i.e., the coldest $\sim 10\%$, or one of nine pixels). When defining 15- and 30-min time-trend fields, this coldest pixel is monitored in three successive 15-min images. Collocation is then needed between the 3×3 VIS–NIR pixels that encompass a cloud (per time and per image), and the 9×9 HRV pixels that cover the same region. Once accomplished, the 9×9 HRV region is processed across all images to obtain the HRV-related fields. In addition to 10.8 μm , the 13.4- μm channel [used in Eq. (4)], is our only use of IR data in this study.

b. Derived fields

Two derived fields were created from the HRV data that describe the BV across a region of developing cumulus clouds: 1) texture estimation and 2) peak detection (PD). In the correlation analysis to follow, both derived BV fields are tested independently of other reflectance channels to identify the presence of visibly bright cumulus clouds against a darker background of ground surfaces under clear-sky conditions, more stratiform-like clouds, and/or the variability in brightness across a small area of active cumulus cloud turrets.

For both BV fields, 15 additional fields are developed using the 9×9 pixel HRV data covering each growing cloud over the three 15-min time periods. Average, maximum, and perturbation BVs are formed for five periods within the three-image set for all 123 convective storms. These five periods are (a) the present image time, (b) the image 15 min in the past, (c) the image 30 min in the past, (d) the 15-min time trend [(a) – (b)], and (e) the 30-min time trend [(a) – (c)]. Both of these 15-min field sets are compared and one form of BV is chosen for further analysis with respect to understanding attributes of growing convective clouds.

For texture (T_{var}) in the HRV data, the variance-based method of Berendes et al. (2008) was followed given the small (9×9 pixel) region being operated on that covers a 3×3 , 3-km VIS–NIR region. Berendes et al. (2008) used texture as one component in the convective cloud mask, cloud typing or identification algorithm used within the SATCAST system. This can be written as

$$T_{\text{var}} = \sum_{k=1}^G (kD_v^2), \quad (6)$$

where G is the number of gray levels in a scene (255 in this application of the HRV data²) and D_v is the

² MSG HRV data are 10 bit, with 1023 unique values. For the computations of brightness variability, the data were scaled linearly to provide 255 brightness levels.

TABLE 1. *Meteosat-9* VIS–NIR interest fields to be evaluated for growing cumulus clouds. The number of fields developed from a given interest field is listed. The physical attribute of a growing cumulus cloud described by each field is on the right. Also, Refl is reflectance and PD is peak detection (see text for definitions of subscripts ave, max, and pert).

CI interest fields	No. of fields	Physical attribute
Refl _{0.6} and time trends ^a	3	Optical depth ^b
Refl _{0.8} and time trends ^a	3	Optical depth ^b
Refl _{1.6} and time trends ^a	3	Cloud-top glaciation, particle size ^b
Refl _{3.9} and time trends ^a	3	Cloud-top glaciation, particle size ^b
PD _{ave} in 9 km × 9 km ^c	3	Clusters of active cumulus clouds
9 km × 9 km time trends ^a of PD _{ave}	2	Clusters of active cumulus clouds
PD _{max} in 9 km × 9 km ^c	3	Discrete clouds and isolated turrets
9 km × 9 km time trends ^a of PD _{max}	2	Discrete clouds and isolate turrets
PD _{pert} in 9 km × 9 km ^c	3	Locally vigorous updrafts
9 km × 9 km time trends ^a of PD _{pert}	2	Locally vigorous updrafts
Total fields	27	

^a Two time trends are considered: 15 and 30 min.

^b Time changes correlate with updraft strength.

^c Present time, and 15 and 30 min previous.

“difference vector” that represents the arithmetical difference between scaled (0–255) 1-km HRV brightness values between two points. This process effectively accumulates the absolute value of the pixel brightness differences in three directions: horizontally, vertically, and diagonally across the 9 km × 9 km HRV region.

For another means of identifying the BV, PD was determined as a difference of Gaussian (DoG) filter approach was applied to HRV data. We followed the methods outlined in Iskenderian et al. (2009) and Wolfson and Clark (2006) for the quantification of convective clouds in advance of CI. For this procedure, a two-dimensional DoG filter was run [with $\sigma = 0$; Marr and Hildreth (1980)], essentially smoothing out the brightness peaks and increasing the brightness in low-brightness regions. Areas with more uniform brightness before applying the DoG filter (e.g., stratiform clouds) remain relatively unaffected. The smoothed image was then subtracted from the original, resulting in an image with no strong cloud-edge gradients, with most of the remaining BV being that associated with “lumpy” convective cloud features. Very high brightness gradients associated with cloud edges are reduced, something that is not accomplished in the texture analysis above.

From these BV values, three fields were created in hopes of representing the utility of this derived quantity. These are the “maximum,” “perturbation,” and “average” BV. Table 1 lists the attributes of the growing convective cloud regions that these three variations of BV should describe. Perturbation BV was computed by taking the difference between the actual pixel value of BV and the average BV (i.e., $BV_{\text{pert}} = BV_{\text{pixel}} - BV_{\text{ave}}$). Maximum BV (BV_{max}) values are simply the largest point value of BV within the 9 × 9 pixel HRV region, whereas BV_{ave} is the average BV in a 9 × 9 pixel region.

After evaluation of a number of cases, the choice was made to focus on the DoG filter PD approach. Two reasons for using the DoG filter method are (a) spurious information associated with sharp edge effects, when bright clouds appear against a dark background, will be suppressed compared to analysis using the texture approach, and (b) cumulus clouds developing in otherwise clear skies, compared to those among a more continuous deck of stratocumulus (for example), will appear more similar in the PD fields; the texture analysis would tend to show these two cases with largely different textural magnitudes.

Figures 1a–d shows how the filter-derived PD is implemented, as in this example, for one time for one growing cumulus cloud event. In Fig. 1a, HRV data covering a 36 km² region with clusters of developing cumulus clouds (bright colors, highlighting the higher brightness) are shown. Data in Fig. 1a are scaled from their original 0–255 brightnesses to 0–120 for better illustration. Figure 1b shows PD (Fig. 1a) after the DoG filter has been applied, while Fig. 1c highlights the PD_{pert} field. In Fig. 1b, regions of convective clouds are highlighted, whereas the surrounding regions are dimmed, and the scale has been reduced by a factor of ~2.67 (values now range from 0 to 45). In Fig. 1d, the single pixel possessing PD_{max} in the filtered image is highlighted (arrow in Fig. 1d), which is that used in the analysis to follow. The process shown in Figs. 1a–d is repeated for every 15-min image in the three-image sequence for all 123 cases analyzed herein.

From the HRV and VIS–NIR reflectance channels, 27 separate so-called interest fields are formed. The 27 total fields are listed in Table 1: 12 reflectance and 15 PD fields.

c. COPS 2007 and case identification

The same COPS dataset used in Part I is analyzed here. The more important components of these data will

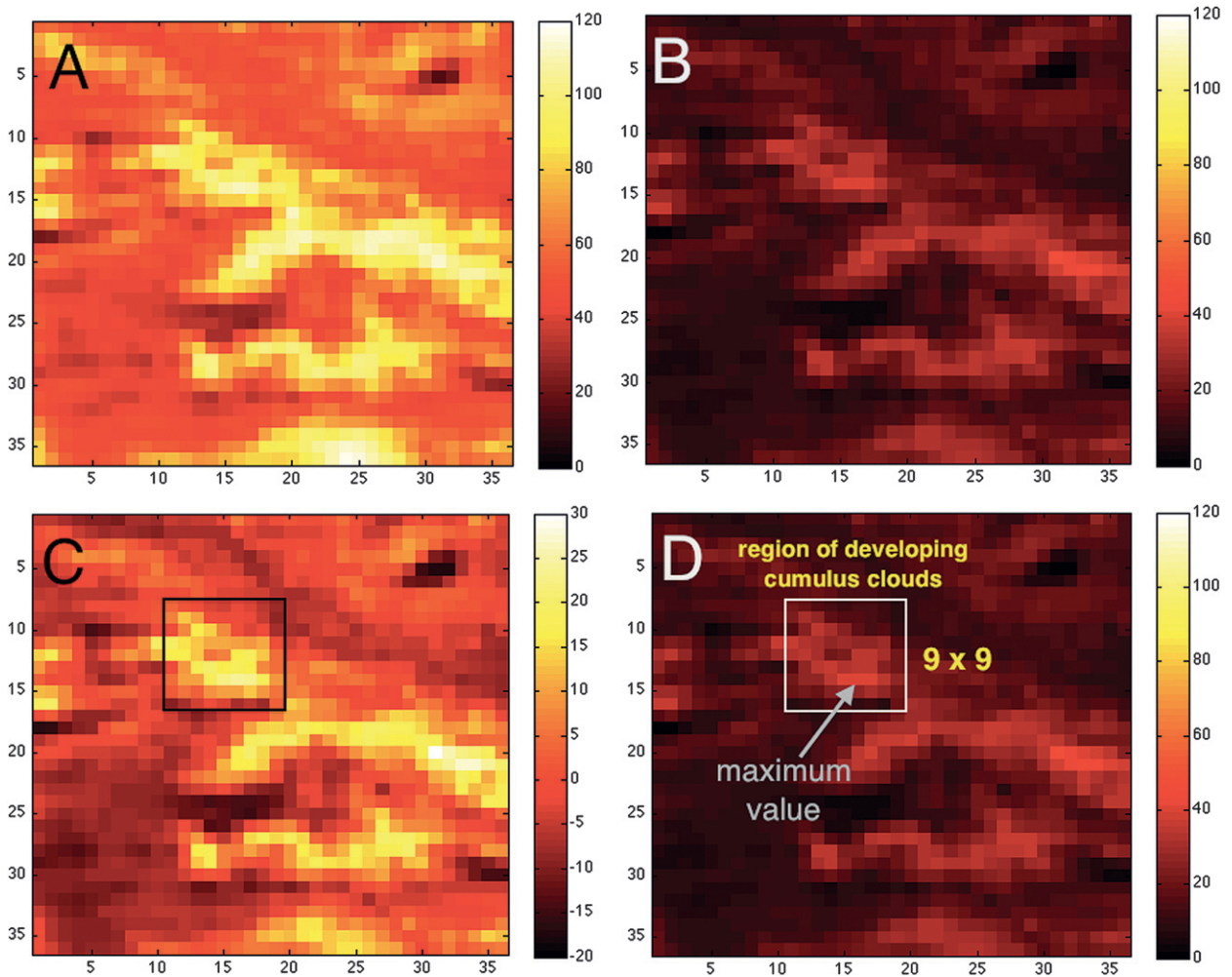


FIG. 1. Example of how the DoG filter brightness PD fields are used for estimating the presence of regions of cumulus clouds with active updrafts. (a) The original 1-km pixel size HRV dataset, scaled from brightnesses 0–120, for better illustration in this example, for a $36 \text{ km} \times 36 \text{ km}$ region containing scattered growing cumulus clouds (light-colored regions are the cumulus clouds). (b) The DoG-filtered PD. Note that the filter effectively smoothes the brightness, while still emphasizing the cumuli seen in (a). (c) Using the mean of all 1296 pixels in (a), perturbation PD (PD_{pert}) values are computed. (d) The manner in which the maximum PD (PD_{max}) value is obtained for one 9×9 , 1-km pixel region centered over a growing convective cloud; i.e., the arrow points to the single pixel containing PD_{max} . The PD_{ave} values are computed as the average PD in the 9×9 pixel box. The PD_{pert} values in (c) are computed only per convective cloud cluster, in the 9×9 boxes seen in (c) and (d) (and hence are evaluated for three images for each 123 events analyzed). Note that the scales are 0–120 in (a), (b), and (d), and –20 to +30 in (c), while the colors may remain similar.

be summarized. The 2007 COPS campaign (Wulfmeyer et al. 2008) was conducted over southern Germany and northeast France from 4 June to 31 August 2007 (information online at www.cops2007.de). The geographical domain was 46.5° – 49.0°N , 6.5° – 11.0°E . One main science goal driving COPS was to increase our understanding of CI as induced in part by orography (Wulfmeyer et al. 2008), and therefore a host of observational data were collected and archived. Two fields in addition to *Meteosat-9* data were used from this archive, those being soundings (collected by the Institut für Meteorologie und Klimaforschung at the Universität Karlsruhe) and dual-polarimetric

radar collected in Waltenheim-sur-Zorn (48.73975°N , 7.61033°E) by the Polarization Diversity Doppler Radar (POLDIRAD) operated by the Deutsches Zentrum für Luft und Raumfahrt (DLR), Institut für Physik der Atmosphäre. Data from several other radars operating over the COPS domain (Karlsruhe, Supersite Rhine Valley, and Supersite Vosges Mountains) were used similarly.

Fifteen days during COPS possessed deep, growing, more isolated cumulus clouds occurring in conditions unobscured by higher clouds. Twenty-six of 88 COPS days were evaluated as they possessed active CI. Table 2 presents the days analyzed, the times on each day over

TABLE 2. COPS 2007 CI days used in this study, with time range and number of CI events per day. Local times are UTC + 1 h for the COPS region.

Date	CI times per day (UTC)	CI events
4 Jun	1142–1557	12
5 Jun	1057–1642	13
8 Jun	0942–1612	15
9 Jun	0927–1457	6
10 Jun	0812–0957	8
11 Jun	1012–1757	15
22 Jun	1342–1627	4
23 Jun	1042–1342	8
12 Jul	1327–1357	2
20 Jul	0942–1827	14
21 Jul	1527–1742	4
24 Jul	1257–1712	6
28 Jul	1457–1812	7
2 Aug	1242–1857	3
3 Aug	1242–1657	6
Total		123

which CI was observed, and the numbers of storms identified and processed. All events were identified by a human expert in channel 9 (10.8 μm) and HRV *Meteosat-9* data. A “high quality” event is defined as clouds growing in mostly clear-sky conditions such that cumuli over a 30-min period could be observed preceding CI without “interference” from higher-level altostratus, altocumulus, or cirrus, which can lead to false identification. For a given good quality day, all 15-min imagery were gathered, and a subset domain for the COPS region was processed from the 3712×3712 IR and 5568×11136 HRV full-disk data. This amounted to processing IR images of 131 elements by 61 lines, and HRV images of 393×183 .

Exactly as in Part I, the goal was to capture cumuli in the *mediocris* (moderate) stage (just beyond the “fair weather” stage) at the initial time, over three successive 15-min images (see Fig. 1 in Part I). Therefore, by the third image in the sequence (e.g., *cumulonimbus calvus*), a new anvil may exist and rainfall may nearly be occurring. Data from the POLDIRAD and other radars were viewed in their native resolution as a means of confirming CI, and for this study, *radar reflectivity simply had to be* ≥ 35 dBZ to be classified as a growing cumulus–CI event. The actual dBZ value ≥ 35 that occurred with a given new storm was not recorded, as this was not part of the study’s goal. Sounding profiles were used to make parallax corrections to the MSG imagery so optimal radar-to-satellite comparisons could be made.

Figure 2 shows examples of the 10.8- μm T_B (Fig. 2a), $\text{Refl}_{0.6}$ (Fig. 2b), $\text{Refl}_{1.6}$ (Fig. 2c), and $\text{Refl}_{3.9}$ (Fig. 2d), as well as HRV imagery (Fig. 2e), over three times (1100, 1115, and 1130 UTC), for a growing cumulus cloud field on 8 June 2007. For Fig. 2, a 3×3 , 3-km pixel-size region in the VIS–NIR and a 9×9 , 1-km pixel-size region

(boxes in Fig. 2) are shown to emphasize the data locations processed as convection grows. From Fig. 2a, the coldest (darkest) 10.8- μm pixel in the 3×3 box is highlighted with a plus sign (+), which is the location where the interest fields are developed. For the PD analysis, data in the entire 9×9 pixel box (Fig. 2e) are processed. The reflectance differences and time changes between the 0.6-, 1.6-, and 3.9- μm channels are substantial in Fig. 2, and this will be discussed below.

4. Results

With 27 initial interest fields available, the motivation of our analysis turned toward 1) determining uniqueness within the data, 2) removing redundant fields and 3) relating all fields to relevant processes occurring in cumulus clouds undergoing growth in advance of CI.

a. Reduction and redundancy

For determining criteria 1 and 2 above, the following procedures were followed. A 27×27 correlation matrix was analyzed. Cases where field-to-field cross correlations were >0.70 were highlighted. High cross correlations between three or more fields were also identified. The result was the removal of several fields that contained redundant information. At this point, the dataset was split into 15 PD and 12 reflectance fields, considering that these explain different attributes of the convective scene.

High correlation (>0.98) was found between all 0.6- and 0.8- μm fields, and both 15- and 30-min time trends (e.g., 30-min trends in 0.6 and 0.8 μm). Therefore, the decision was made to not consider all 0.8- μm -related fields, which resulted in removing 3 of the 12 reflectance fields. Use of the 0.6- versus 0.8- μm data was chosen because the latter are more proven in previous studies as a means of estimating the optical depth in clouds (Nakajima and King 1990). The remaining nine interest fields were then subject to principal component analysis (PCA; Johnson and Wichern 2002) as described below.

Very high correlations (>0.95) were also found between all three types of PD (PD_{pert} , PD_{ave} , and PD_{max} , in a 9×9 HRV box), as well as between the two time trends for all three BV fields. After consideration of the differences and attributes of PD_{max} and PD_{pert} , it was determined that PD_{ave} would be most valuable. This is supported by Wolfson and Clark (2006), who use PD_{ave} , and hence this is a more proven field. Using only PD_{ave} resulted in the loss of 10 fields from the original 15 HRV-related fields. Table 3 presents the remaining, less correlated fields.

b. PCA

Given nine reflectance and five BV interest fields, PCA was subsequently performed on each separately. The goals of using PCA are to help further quantify field

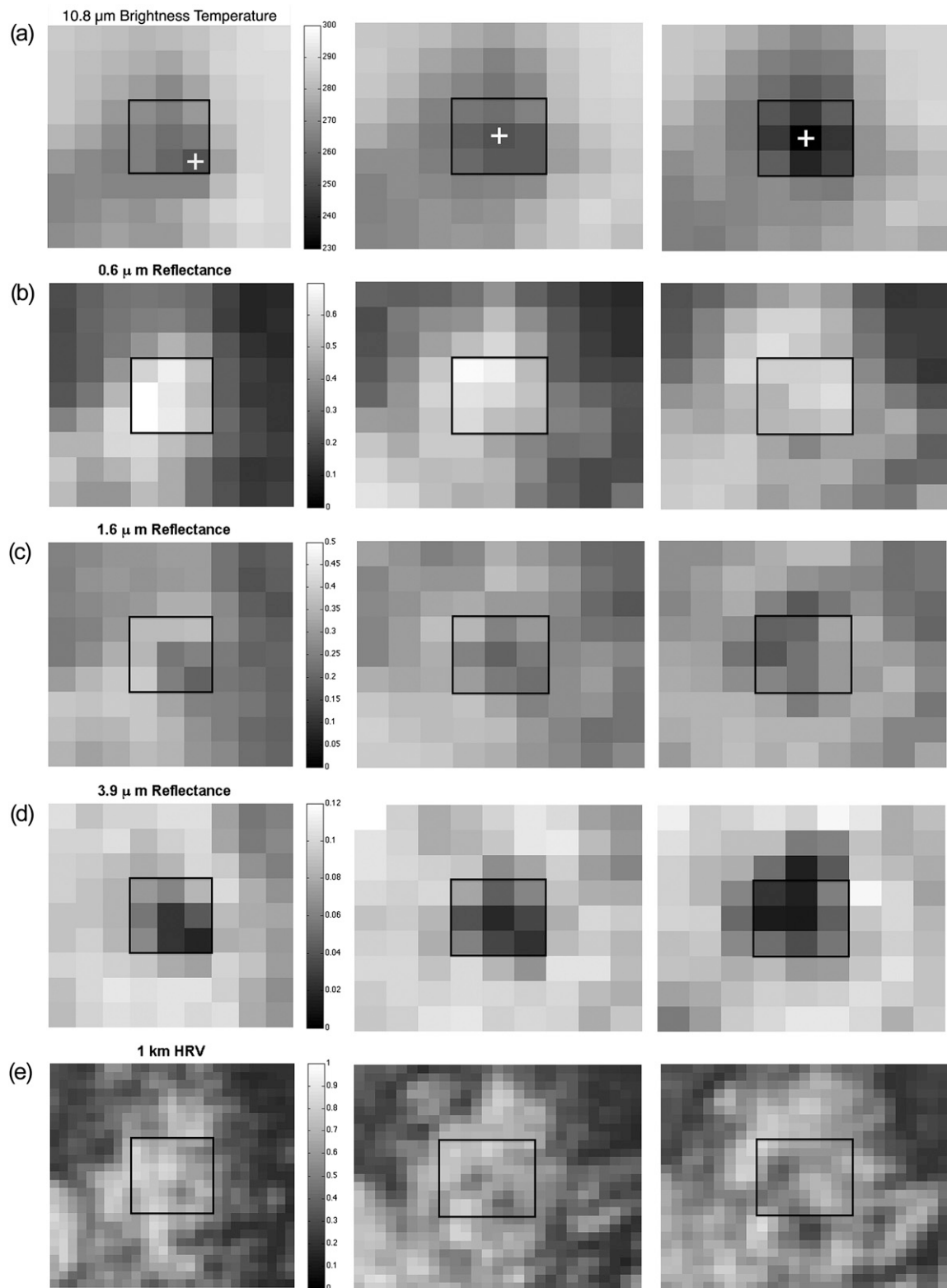


FIG. 2. An example of one CI event (1 storm among the 123) at (left to right) 1100, 1115, and 1130 UTC 8 Jun 2007. Shown are (a) 10.8- μm brightness temperature, T_B ; (b) $\text{Refl}_{0.6}$; (c) $\text{Refl}_{1.6}$; (d) $\text{Refl}_{3.9}$; and (e) 1-km sampling distance HRV data. For (d), Eq. (1) was used to convert to reflectances. In all images, squares denote the region over which the data were analyzed with respect to the coldest IR pixel [plus sign in (a)]. See text for discussion.

TABLE 3. VIS–NIR interest fields that do not contain redundant information (from those in Table 1) for describing cumulus cloud growth. Here, nonredundant implies correlation coefficients <0.70 when compared against all other fields. For each field, the “critical value” or tendency of the field as measured over growing cumulus is provided. Abbreviations are as in Table 1. The statement “relatively high within distribution” refers to the field magnitude being large when compared with values within a population (i.e., a distribution) of convective clouds.

Interest fields	No. of fields	Critical value ^a
Refl _{0,6} and time trends ^a	3	Unknown
Refl _{1,6} and time trends ^a	3	Unknown
Refl _{3,9} and time trends ^a	3	Decrease to $\leq 5\%$ ^b
PD _{ave} in 9 km \times 9 km current time	1	Higher within distribution
PD _{ave} in 9 km \times 9 km 15 min previous	1	Relatively high within distribution
PD _{ave} in 9 km \times 9 km 30 min previous	1	Relatively high within distribution
PD _{pert} in 9 km \times 9 km current time	1	Relatively high within distribution
PD _{pert} in 9 km \times 9 km 15 min previous	1	Relatively high within distribution
Total fields	14	

^a Two time trends are considered: 15 and 30 min.

^b Rosenfeld et al. (2008); Harris et al. (2010).

redundancy and to establish a level of field uniqueness for describing the given outcome or event (substantial cumulus cloud development prior to CI). Given that the units of all interest fields were either reflectivity, the change in reflectivity, PD, or the change in PD, data normalization was done in this PCA using the *correlation* matrix [as opposed to the covariance matrix; Wilks (2006)]. Without the normalization the correlation matrix provides, data with larger magnitudes (e.g., K versus reflectances from 0 to 1) will artificially contribute more to the explained variance.

Table 4 presents the PCA results for reflectance, while Table 5 presents the PD fields. Rankings are determined from the PCA, specifically the size of the eigenvalues in principal component 1 and, if needed, component 2. The rankings *may* be used as a means of weighting each interest field in terms of importance when describing a given attribute or process, per MSG pixel, or per cumulus cloud object. Later, suggestions are provided on how to utilize these fields in 0–1-h CI nowcasting applications. From Table 4, the 30-min trend in Refl_{3,9} is the most important field when describing convective cloud development. This is followed by the 30-min trend in Refl_{1,6}, the 15-min trend

in Refl_{3,9}, the 15-min trend in Refl_{1,6}, and the instantaneous Refl_{3,9} and Refl_{1,6}. From Table 5, PD_{ave} 15 and 30 min prior to the latest image time are the two most important fields, while the present-time PD_{ave} values are third in importance.

As a means of verifying that the results in Tables 4 and 5 are robust, the correlation and PCA analyses were repeated using a dataset in which a random 20% of the storms were removed. The PD fields were unchanged from those in Table 5, and therefore Table 6 shows the reflectance fields only when 100 events were analyzed. Little overall change is noted. Fields that ranked in the top three for the whole dataset remained of the same importance. The rankings for the 15-min trend in Refl_{1,6} and Refl_{3,9} switched, and instantaneous Refl_{1,6} replaced the Refl_{0,6}, as shown in Table 4. Given the similarities between Tables 4 and 6, the top five reflectance fields are shown to be robust.

c. Physical attribute relationships

Table 1 briefly summarizes the physical interpretation of a given interest field with respect to growing cumulus clouds. Specifically, however, what does each interest field

TABLE 4. PCAs of the top six reflectance fields using $A_{s,z}$ -normalized VIS–NIR data. The method for reduction to six fields within all the VIS data is described in the text. For this PCA, the correlation matrix was used, and the cumulative proportion of the explained variance (ExpVar) is listed. Only the first six components are shown. A blank in the component (comp) column signifies an insignificant value (<0.100). The rank of the fields, in terms of uniqueness to the assessment of cloud depth in this case, is shown in the far-left column.

Rank	Interest fields	Comp 1	Comp 2	Comp 3	Comp 4	Comp 5	Comp 6
1	30-min trend Refl _{3,9}	0.514	0.123		0.162	0.484	−0.679
2	30-min trend Refl _{1,6}	0.464		0.163	0.701		0.515
3	15-min trend Refl _{3,9}	0.444	−0.298	−0.200	−0.553	0.413	0.444
4	15-min trend Refl _{1,6}	0.389	−0.528	−0.293		−0.645	−0.259
5	Refl _{3,9}	0.354	0.291	0.711	−0.404	−0.347	
6	Refl _{0,6}	−0.216	−0.729	0.585	0.112	0.241	
	ExpVar	0.520	0.698	0.824	0.917	0.979	1.000

TABLE 5. PCA of PD fields from A_{sz} -normalized HRV data. The method for reduction to five PD fields is described in the text. For this PCA, the correlation matrix was used, and the cumulative proportion of the explained variance (ExpVar) is listed. The rank of the fields, in terms of uniqueness to the assessment of cloud depth in this case, is shown in the far-left column.

Rank	Interest fields	Comp 1	Comp 2	Comp 3	Comp 4	Comp 5
1	PD _{ave} 15 min previous	-0.495	0.366	-0.116	-0.176	-0.759
2	PD _{ave} 30 min previous	-0.464	0.483		0.615	0.407
3	PD _{ave} current time	-0.450	-0.290	-0.628	-0.442	0.353
4	PD _{pert} 15 min previous	-0.447		0.753	-0.400	0.270
5	PD _{pert} current time	-0.371	-0.741	0.127	0.486	-0.247
	ExpVar	0.620	0.802	0.918	0.944	1.000

provide that is unique to describing growing cumulus clouds prior to CI? Other questions from the results in Tables 4–6 include the following: 1) What do the $Refl_{0.6}$, $Refl_{1.6}$, and $Refl_{3.9}$ provide in such an analysis about cloud-top properties? 2) What do PD_{ave} and PD_{pert} explain with respect to growing convective clouds? 3) How can these results be applied when monitoring active convective clouds in HRV, VIS, and NIR data prior to CI?

In general, the differences between the 0.6-, 1.6-, and 3.9- μm channel data observations are related to (a) scattering properties of ice versus liquid water hydrometeors, (b) changes in optical depth, and (c) the increase in hydrometeor size as clouds grow and persist. Reflectance changes that correlate to the transition to mainly ice hydrometeors, and to particle size (effective radius) increases that accompany cloud-top glaciation, are observed in the 1.6- and 3.9- μm data. Optical depth changes can be estimated from changes in the 0.6- μm channel (Baum et al. 2000a,b; Greenwald and Christopher 2000), yet for the “optically thick” convective clouds being analyzed here, less sensitivity is expected (as seen in Fig. 1b, cf. with Figs. 1c and 1d). Greenwald and Christopher (2000) show that changes in $Refl_{1.6}$ are associated with changes from water to ice hydrometeors. Nakajima and King (1990) show that both the $Refl_{1.6}$ and $Refl_{3.9}$ (and associated time changes) are correlated with the effective radii of particles for both liquid and water hydrometeors. Therefore, as a cumulus cloud’s main updraft region partially or completely glaciates, $Refl_{1.6}$ and $Refl_{3.9}$ will drop as ice particles form and their sizes increase significantly. The reflectance

(-drop) signature from the 1.6- μm channel is found to be more immediate and larger initially when compared with the $Refl_{3.9}$ as glaciation first occurs, yet as clouds deepen and larger particles form (into the $\geq 10\text{-}\mu\text{m}$ range), $Refl_{3.9}$ is seen to fall more quickly (Nakajima and King 1990).

For $Refl_{3.9}$ signatures, cloud-to-cloud variability has been correlated with updraft velocity and storm intensity, and hence the time particles have to grow prior to freezing (Levizzani and Setvák 1996; Lensky and Rosenfeld 2008; Rosenfeld et al. 2008). Additionally, $Refl_{3.9}$ will vary with cloud condensation nuclei (or aerosols) concentrations and cloud-base temperature (via changes in particle size). As documented then, 3.9- μm (and likely 1.6 μm) information will possess more variability between cumulus clouds as local storm environments influence instability, updraft strength, and cloud microphysics. Updraft strength can subsequently be inferred in time trends in $Refl_{1.6}$ and $Refl_{3.9}$, in part due to decreases in particle sizes at cloud top, as shown in Setvák et al. (2003).

As a means of directly comparing the $Refl_{0.6}$, $Refl_{1.6}$, and $Refl_{3.9}$, Figs. 3a–d show scatterplots of these data at the third time in the sequence of images, only for the coldest pixel in the 3×3 pixel area per convective cloud. In Figs. 3a–c, colors correspond to the 10.8- μm T_B , which allows us to understand these relationships as a function of cloud depth, cloud-top temperature, and the likely presence of ice. For Fig. 3a, the relationship between 0.6 and 1.6 μm is shown, which is contrasted with Fig. 3b. In Fig. 3a, in general, as cloud tops cool, 1.6- μm reflectance decreases, while the $Refl_{0.6}$ remains highly variable. The scatter is

TABLE 6. As in Table 4, but for a dataset in which 20% of the storms were randomly removed from the 123-storm set (using only 100 storms). Note that the ranks of fields 4–6 have changed, with fields 4 and 5 in Table 4 switched, and the $Refl_{1.6}$ replaced $Refl_{0.6}$ in the sixth position.

Rank	Interest fields	Comp 1	Comp 2	Comp 3	Comp 4	Comp 5	Comp 6
1	30-min trend $Refl_{3.9}$	-0.485	-0.165	0.475	0.132		0.700
2	30-min trend $Refl_{1.6}$	-0.465		0.367	-0.601	-0.227	-0.485
3	15-min trend $Refl_{3.9}$	-0.426	-0.325	-0.258	0.613	-0.386	-0.349
4	$Refl_{3.9}$	-0.399	0.497	0.122	0.311	0.652	-0.240
5	15-min trend $Refl_{1.6}$	-0.382	-0.370	-0.622	-0.367	0.405	0.178
6	$Refl_{1.6}$	-0.248	0.695	-0.414	-0.120	-0.453	0.253
	ExpVar	0.538	0.756	0.860	0.942	0.981	1.000

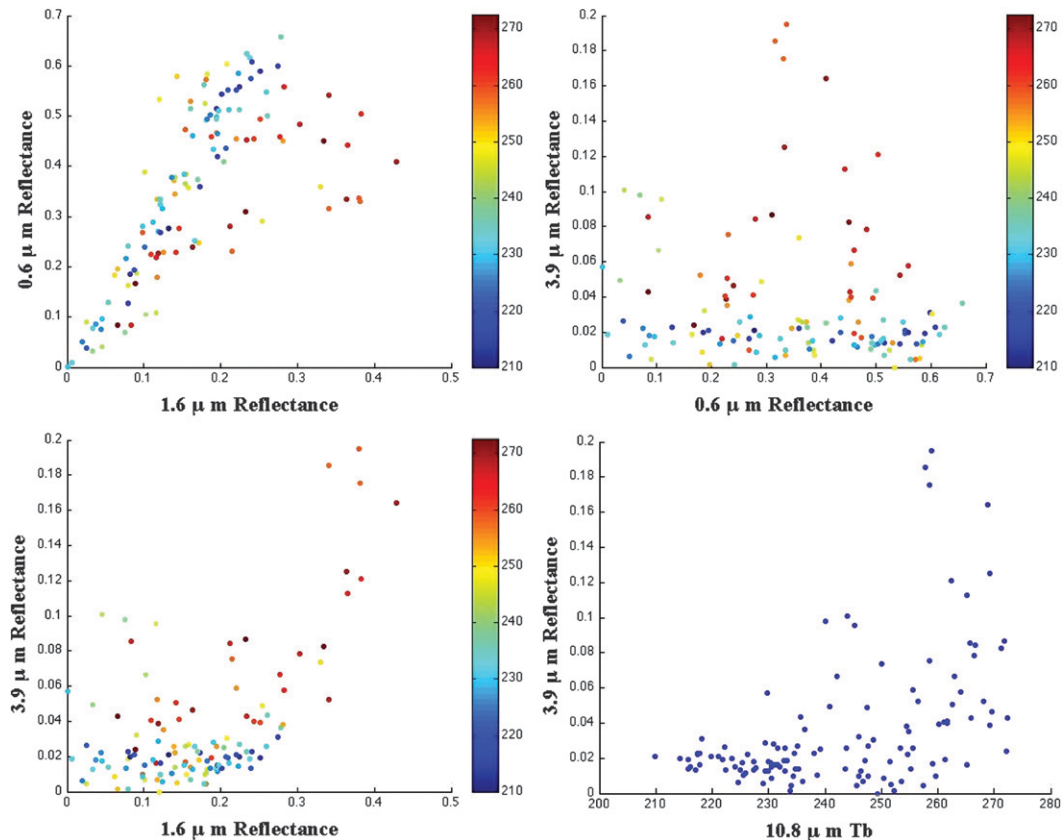


FIG. 3. Scatterplots for solar reflectance fields. Reflectances of (a) 1.6 vs 0.6, (b) 0.6 vs 3.9, (c) 1.6 vs 3.9 μm , and (d) $\text{Refl}_{3.9}$ vs 10.8- μm T_B . Data are colored according to the coldest 10.8- μm T_B (K) in the 3×3 pixel area analyzed per convective cloud. An individual point represents 1 of the 123 events that occurred during COPS 2007. See text for interpretation.

somewhat larger for warmer clouds as effective radii of particles remain small. The wide variance in $\text{Refl}_{0.6}$ suggests that, with large optical depths for all clouds studied ($\gg 1$), the roughnesses of cloud tops remain similar as they grow. (The 0.6- μm reflectance is known to be more or less independent of particle size.) Also, as the amount of cumulus cloud occupying a 3-km pixel, or its horizontal extent, increases, so will $\text{Refl}_{0.6}$ simply because the amount of cloud in the scene increases.

In Figs. 3b and 3d, low (<3%) $\text{Refl}_{3.9}$ are also associated with colder, glaciated cloud tops and the presence of larger ice particles [to as large as 30–70 μm ; Levizzani and Setvák (1996)], while again the 0.6- μm values do not vary as a function of cloud-top T_B . Because of the positive correlation between glaciation and optical depth (Baum et al. 2000a), the 1.6- and 0.6- μm channels are more linearly related, with increasing optical depth ($\text{Refl}_{0.6}$) correlating with increased ice hydrometeors ($\text{Refl}_{1.6}$), with lesser correlations with warmer clouds.

Figure 3c illustrates the relationship between $\text{Refl}_{1.6}$ and $\text{Refl}_{3.9}$, which shows that as ice hydrometeors form, $\text{Refl}_{3.9}$ drops significantly, being mostly below 3% when cloud-

top T_B s are below 235 K. The $\text{Refl}_{1.6}$ decreases to mainly <25% for clouds below 240 K, however, not exclusively. The lack of a 1:1 relationship in Fig. 3c is caused by differences in the indices of refraction at both wavelengths, which vary between ice and water to also make the single-scattering albedos different. There is some sensitivity of $\text{Refl}_{1.6}$ and $\text{Refl}_{3.9}$ to particle sizes, yet we expect this to be small. From Figs. 3a–d we conclude that use of both the 1.6- and 3.9- μm channels (the top four fields in Table 4) provides us with unique tests for glaciation and associated particle size changes, which subsequently can be related to the CI process when ice is important in precipitation formation. It is also clear that reflectance from the 0.6- μm channel provides less definitive information about cloud-top character, hence it being least important (Table 4), yet it can be used to confirm that a cloud is optically thick and hence that use of $\text{Refl}_{3.9}$ is acceptable.

From Table 5, the three top PD fields show that the presence of active up- and downdrafts within isolated or clustered cumulus clouds are important indicators of rapidly growing cumulus. High PD 15 and 30 min prior to the current time, and at the current time, imply active

TABLE 7. Mean and SD values for the VIS–NIR “interest fields” in Tables 4 and 5—the IR that describe cumulus cloud-top glaciation through reflectance changes. Fields are listed in order of the ranking as shown in Tables 4 and 5. Mean and SD are in fractional reflectance, from 0 to 1. Units of the PD fields are in brightness counts (0–255). Higher PD (“peakiness”) will occur within a field of “lumpy,” developing cumulus clouds vs cumulus with weaker updrafts that are developing more slowly and have smoother tops.

Rank	Interest fields	Mean	SD
1	30-min trend Re _{fl} _{3.9}	−0.0264	0.041
2	30-min trend Re _{fl} _{1.6}	−0.0480	0.069
3	15-min trend Re _{fl} _{3.9}	−0.0081	0.026
4	15-min trend Re _{fl} _{1.6}	−0.0083	0.040
5	Re _{fl} _{3.9}	0.0362	0.038
6	Re _{fl} _{0.6}	0.3552	0.172
1	9 × 9 PD _{ave} 15 min previous	30.50	31.8
2	9 × 9 PD _{ave} 30 min previous	29.24	27.9
3	9 × 9 PD _{ave} current time	24.24	21.4
4	9 × 9 PD _{pert} 15 min previous	16.17	17.4
5	9 × 9 PD _{pert} current time	16.27	15.1

convective updrafts, and exceptionally lumpy clouds (as opposed to more smooth-topped clouds that accompany stratiform clouds). The perturbation values at 15 min prior to, and at, the current image time compose the remaining fields. These latter two fields help describe the presence of either locally tall and isolated turrets, or simply the existence of one main towering cumulus cloud updraft.

Table 7 lists the mean and standard deviation (SD) values of the retained interest fields. Note that the SD values are often much larger than the mean values, sometimes by a factor of 2–3. This implies a wide range of variability in all reflectance and PD fields across this population of growing cumulus clouds, quite likely related to varying convective environments on the COPS days studied.

Next, we examine the subset of clouds that were relatively warm at the third image time, as was done in Part I. Growing cumulus cloud events in which the cloud tops remained ≥ 240 K were analyzed separately, with the results presented in Table 8. Several interesting conclusions can be drawn when comparing Tables 7 and 8. First, whereas the Re_{fl}_{0.6} field is of minimal importance in describing clouds over the entire dataset, for warmer-topped clouds it becomes an important and unique field. For cumuli either growing and nonglaciated, or just beginning to glaciate, the two time trends in Re_{fl}_{0.6} are positive, in contrast to negative reflectance trends seen at 1.6 and 3.9 μm . The high brightness (35%) seen in Table 7 for the instantaneous Re_{fl}_{0.6} seems to be consistent with the upward trend in this field seen in the top two fields in Table 8. This implies that increasingly lumpy, visibly bright clouds are associated with active convection, and (as noted above) that Re_{fl}_{0.6} will

TABLE 8. As in Table 7, but for clouds with cloud-top temperatures ≥ 240 K. Note that the rankings determined from PCA have changed when compared with those in Tables 4 and 5, suggesting field variability as clouds grow and cool in this warmer subset of clouds. See text for discussion.

Rank	Interest fields	Mean	SD
1	30-min trend Re _{fl} _{0.6}	0.0124	0.077
2	15-min trend Re _{fl} _{0.6}	0.0071	0.051
3	30-min trend Re _{fl} _{1.6}	−0.0214	0.059
4	15-min trend Re _{fl} _{1.6}	−0.0670	0.035
5	Re _{fl} _{3.9}	0.0273	0.042
6	Re _{fl} _{1.6}	0.1238	0.104
1	9 × 9 PD _{ave} 30 min previous	14.89	22.0
2	9 × 9 PD _{ave} 15 min previous	16.00	25.0
3	9 × 9 PD _{ave} current time	14.07	21.2
4	9 × 9 PD _{pert} 15 min previous	9.66	15.6
5	9 × 9 PD _{pert} 30 min previous	9.20	16.0

increase as clouds occupy more of a single 3-km pixel as they increase in horizontal extent. The 1.6- μm trends in reflectance remain negative (as in Table 7), yet again they fall behind the 0.6- μm fields in terms of importance. Also in Table 8, the top three PD fields remain nearly the same as that seen for the entire dataset, with PD_{pert} 30 min previous to the latest image in the sequence replacing the present-time PD_{pert}, as seen in Table 7.

d. Application of results

Methods for using the information provided in Tables 7 and 8 are proposed in an analogous way to that presented in Part I. When using MSG’s VIS–NIR data alone in nowcasting growing cumulus clouds toward CI, weighting each field along the lines of the rankings in Tables 4, 5, 7, and 8 while assuming normalization between 0 and 1 is one possible approach of threshold-based tests. Another method would be to score a cumulus cloud object from 0 to 11 for cloud-top glaciation, and then combine this with information determined from the IR interest fields (Part I). For estimating CI likelihood for individual convective clouds (per pixel, or per cluster of pixels), use of the mean values to define a range per interest field that accounts for nonlinearities between HRV and VIS–NIR observations and physical processes (i.e., glaciation, hydrometeor size variability) would be a practical application. This was the method used when implementing the algorithm as described in Mecikalski and Bedka (2006) and Siewert et al. (2010).

To help estimate a range of values per interest field, one may add or subtract (whichever is appropriate) $\frac{1}{2}$ to 1 SD from the mean value, per field. For example, a critical value for the 30-min Re_{fl}_{3.9} trend might be -0.026 ± 0.041 , or -0.014 to -0.067 (or a 30-min reflectance decrease of ~ 1.4 – 6.7%), or defining the “critical” value for the 30-min Re_{fl}_{1.6} trend to be between -0.021 and -0.117

(from -2.1% to -11.7% per 30 min; -0.048 ± 0.069). Use of null events (in which clouds failed to CI or continue developing) should be done to help set optimal threshold values.

Convective environments [or convective regimes; Boccippio et al. (2005); Li et al. (2006)] vary considerably in space and time; therefore, being aware that growing cumulus clouds will exhibit different cloud-top signatures in reflectance and BV is important. This is caused by 1) variation in aerosols, which influence the scattering and attenuation of visible light returning to the *Meteosat-9* sensor; 2) the local freezing altitude, which impacts cloud-top glaciation rates and hence the reflective properties of newly glaciated clouds; and 3) instability, the amount of convective available potential energy (CAPE), and its vertical profile, which influences updraft velocity directly and, indirectly, the spectral signature of glaciation via cloud-top microphysics (Setvák and Doswell 1991; Rosenfeld et al. 2008; Lensky and Rosenfeld 2008). High instability (i.e., high CAPE) and vertical variations in stability should enhance BV as distinct, vigorous cloud turrets will be present within a scene.

More sophisticated procedures for using HRV and VIS–NIR data would involve the creation of histograms relating interest field values and environmental factors (e.g., vertical temperature and/or moisture profiles), developing empirical relationships, and subsequently determining the likelihood of CI. This method is similar to an ensemble approach and would require the analysis of a substantial number of events such that a robust statistical model or empirical function could be formulated. Depending on whether or not the “rate of CI” is important, critical thresholds may be increased or decreased accordingly based on relationships to known aspects of the convective environment in which the cumulus clouds are embedded, perhaps allowing for different weights to be placed on fields as a function of the atmospheric characteristics. Specifying a variable range in interest field-specific “critical” thresholds as a function of environmental conditions is another way of accounting for these factors. Environmental information can come from regional numerical weather prediction models (e.g., the European Centre for Medium-Range Weather Forecasts, ECMWF), via passive microwave remote sensing retrievals (which possess a much larger field of view), or also from IR with $\sim(3\text{--}6)\text{-h}$ sampling times (e.g., the Atmospheric Infrared Sounder, AIRS).

PD fields can identify rapidly growing updrafts (a lumpy appearance in the imagery), allowing a user to discern between convective and nonconvective clouds in an unstable environment. In cases of nonconvective, stratocumulus, or cumuliform clouds, when weaker updrafts are providing the main cloud-growth signals, low PD values will

be obtained. Low PD situations can then be evaluated more carefully, leading to a reduction in the false detection of new CI when other VIS, NIR, and IR information is used.

e. Error sources

Because of the relatively large sample size (123 events), most of the main statistical signals should be well represented. Yet, errors do exist. The main sources of error in this study are summarized as follows. First, as in Part I, since the events used in this study were determined subjectively, it is likely that several of the 123 CI cases are not ideally oriented in time and space relative to the *Meteosat-9* data used. Specifically, it is possible that at the initial time (of a sequence of three, 15-min images) the cumulus clouds may have already reached the “towering” cumulus stage, and by the third image in the sequence, rainfall (a $\geq 35\text{-dBZ}$ echo) may have already occurred. In these cases, the physical processes of growing cumuli related to the *Meteosat-9* data would still be captured, yet several of the trend fields may be erroneous as the cloud would have possessed an anvil. Second, the subjective determination of cumulus cloud types in a three-image sequence is sometimes incorrect, and nonconvective clouds would be analyzed instead to define the interest fields. This is caused by challenges involved in identifying cumulus in 1-km HRV data and 3-km pixels.

Other errors are associated with view angle influences over the COPS domain. With the southern edge of this domain at 46.5° , high view angles exacerbate the interpretation of cloud types from MSG data, which can lead to some false determination of the size of the pre-CI convective clouds as a significant portion of the sides of cumulus clouds are viewed (dulling the “cloud top” signal). A third source of error is the likelihood that higher-level cirrus clouds obscured lower cumuli in some of the images used per case, which will weaken the observed VIS–NIR cloud-top signatures with respect to solar reflectance. Also, error caused by the inadequate ground-based radar observations of a given new thunderstorm development over the COPS domain will influence the precise time determination of CI (and hence the proper image set used per event to define the interest fields). Finally, it is very possible that some CI events never achieved $>35\text{-dBZ}$ echo intensity, because of dry environments or poor radar observations. Errors caused by misregistration between the HRV and VIS–NIR fields are not expected to be a source of error (see Schmetz et al. 2002).

5. Conclusions

A total of 27 IR CI interest fields are initially assessed for the level of reflected and BV information they contain. The reflectance fields ultimately help determine cloud-top

glaciation, related in many cases to changes in particle size and the formation of ice hydrometeors, while BV fields diagnose the presence of active convective clouds, which further correlate to updraft vigor. Through correlation and principal component analyses, 11 fields (5 PD, 6 reflectances) out of 27 initial fields are identified as containing the least amount of redundant information. The main findings include the following key points. 1) Time trends of decreasing $\text{Refl}_{1.6}$ and $\text{Refl}_{3.9}$ correlate well to growing cumulus clouds undergoing CI, with 15-min trends of reflectance being near -0.83% to -0.81% for both channels. Thirty-minute trends for $\text{Refl}_{1.6}$ and $\text{Refl}_{3.9}$ are -4.8% and -2.6% , respectively. 2) Cloud-top reflectances at or below $\sim(3.6\text{--}3.5)\%$ as measured at $3.9\ \mu\text{m}$ appear to be a good indicator that ice hydrometeors are in abundance, and a phase change has occurred. 3) Higher PD indicates the presence of a cumulus field or the highly nonuniform brightnesses produced by cumuli against an otherwise darker or uniform background. 4) Data in the highly correlated 0.6- and 0.8- μm channels, although indicators of optical depth changes as clouds deepen, appear to be insensitive to cloud development and are not valuable indicators alone of growing convective clouds. Yet, (5) $\text{Refl}_{0.6}$ and its time rate of change, have more value for describing cloud-top conditions for warmer, lower cumulus clouds as compared to clouds more likely to contain significant percentages of ice hydrometeors. Several methods are proposed on how growing convective clouds may be quantified per cumulus cloud “object,” toward monitoring cumulus cloud growth rates, and to perhaps nowcast CI over 1-h time frames.

This research becomes important when one looks into the near future of geostationary meteorological satellite technology over much of Earth, specifically for the forthcoming Meteosat Third Generation (MTG), the Advanced Baseline Imager (ABI) aboard the GOES-R series of GOES satellites (Schmit et al. 2005, 2008), and other high spectral resolution geostationary imagers supported by other countries [e.g., China’s Fengyun (FY) -3 and -4 satellites, Japan’s Hinawari-8 scheduled for 2014]. These results should help to better define how several channels containing reflectance and BV information can be considered for use within thunderstorm nowcast systems. These include the Corridor Integrated Weather System (CIWS; Wolfson and Clark 2006), the Thunderstorm Identification, Tracking, and Nowcasting (TITAN; Han et al. 2009), the Rapid Development Thunderstorms (Guillou 2008), the Cumulonimbus Tracking and Monitoring (Cb-TRAM; Zinner et al. 2008), and those as reviewed in Wilson et al. (2004).

Future work will involve testing the above results within algorithms that monitor convective clouds over time, or within CI nowcast systems similar to those listed

above. An evaluation of a wide range of cases will be necessary to properly determine errors, especially “null” events where cumulus clouds evolved as predicted by HRV, VIS, and NIR interest field observations yet rainfall never reached a critical intensity (i.e., a thunderstorm never developed). Siewert et al. (2010) represent one preliminary study in which the IR fields are tested in a validation effort; however, more extensive work is required, coupling the IR, VIS–NIR, and HRV portions of the *Meteosat-9* dataset. Follow-on work will also involve the use of retrieved cloud-top microphysical quantities like effective radius, optical thickness, ice water path, and cloud phase as a means of gauging in-cloud updraft strength and subsequently storm intensity, along the lines of Lensky and Rosenfeld (2008).

Acknowledgments. This project was funded by the European Organisation for the Exploitation of Meteorological Satellites (EUMETSAT), Contract EUM/CO/08/4600000538/MK. We also thank Dr. Haig Iskenderian from the Massachusetts Institute of Technology, Lincoln Laboratory, for the use of the two-dimensional DoG filter algorithm. This paper’s quality was significantly improved through the comments of three anonymous reviewers. We also thank Phil Watts (EUMETSAT) for a valuable review of this document.

REFERENCES

- Adler, R. F., and R. A. Mack, 1986: Thunderstorm cloud top dynamics as inferred from satellite observations and a cloud top parcel model. *J. Atmos. Sci.*, **43**, 1945–1960.
- Baum, B. A., V. Tovinkere, J. Titlow, and R. M. Welch, 1997: Automated cloud classification of global AVHRR data using a fuzzy logic approach. *J. Appl. Meteor.*, **36**, 1519–1540.
- , D. P. Kratz, P. Yang, S. Ou, Y. Hu, P. F. Soulen, and S.-C. Tsay, 2000a: Remote sensing of cloud properties using MODIS airborne simulator imagery during SUCCESS. 1. Data and models. *J. Geophys. Res.*, **105** (D9), 11 767–11 780.
- , P. F. Soulen, K. I. Strabala, M. D. King, S. A. Ackerman, W. P. Menzel, and P. Yang, 2000b: Remote sensing of cloud properties using MODIS airborne simulator imagery during SUCCESS. 2. Cloud thermodynamic phase. *J. Geophys. Res.*, **105** (D5), 11 781–11 792.
- Berendes, T. A., J. R. Mecikalski, W. M. Mackenzie Jr., K. M. Bedka, and U. S. Nair, 2008: Convective cloud identification and classification in daytime satellite imagery using standard deviation limited adaptive clustering. *J. Geophys. Res.*, **113**, D20207, doi:10.1029/2008JD010287.
- Boccippio, D. J., W. A. Petersen, and D. J. Cecil, 2005: The tropical convective spectrum. Part I: Archetypal vertical structures. *J. Climate*, **18**, 2744–2769.
- Ebert, E., 1987: A pattern recognition technique for distinguishing surface and cloud types in the polar regions. *J. Appl. Meteor.*, **26**, 1412–1427.
- EUMETSAT, 2007: MSG level 1.5 image data format description. EUMETSAT Publ. EUM/MSG/ICD/105, 122 pp. [Available from EUMETSAT, Am Kavalleriesand 31, D-64295 Darmstadt, Germany.]

- Greenwald, T. J., and S. A. Christopher, 2000: The GOES IM imagers: New tools for studying microphysical properties of boundary layer stratiform clouds. *Bull. Amer. Meteor. Soc.*, **81**, 2607–2619.
- Guillou, Y., 2008: Algorithm theoretical basis document for rapid development thunderstorms. RDT-PGE11 version 2.0, Météo-France, 61 pp.
- Gurka, J. J., 1986: Satellite and surface observations of strong wind zones accompanying thunderstorms. *Precipitation and Convection*, Vol. 2, *Satellite Imagery Interpretation for Forecasters*, Meteor. Monogr., National Weather Association, 4-L-1–4-L-8.
- Han, L., Y. Zheng, H. Wang, and Y. Lin, 2009: 3D convective storm identification, tracking and forecasting—An enhanced TITAN algorithm. *J. Atmos. Oceanic Technol.*, **26**, 719–732.
- Harris, R. J., J. R. Mecikalski, W. M. MacKenzie Jr., P. A. Durkee, and K. E. Nielsen, 2010: The definition of GOES infrared lightning initiation interest fields. *J. Appl. Meteor. Climatol.*, **49**, 2527–2543.
- Heidinger, A. K., R. Frey, and M. J. Pavolonis, 2004: Relative merits of the 1.6 and 3.75 micron channels of the AVHRR/3 for cloud detection. *Can. J. Remote Sens.*, **30**, 182–194.
- Hunt, G. E., 1973: Radiative properties of terrestrial clouds at visible and infra-red thermal window wavelengths. *Quart. J. Roy. Meteor. Soc.*, **99**, 346–369.
- Hutchison, K. D., J. K. Roskovensky, J. M. Jackson, A. K. Heidinger, T. J. Kopp, M. J. Pavolonis, and R. Frey, 2005: Automated cloud detection and classification of data collected by the Visible Infrared Imager Radiometer Suite (VIIRS). *Int. J. Remote Sens.*, **26**, 4681–4706.
- Isaacs, R., and J. Barnes, 1987: Intercomparison of cloud imagery from the DMSP OLS, NOAA AVHRR, GOES VISSR, and Landsat MSS. *J. Atmos. Oceanic Technol.*, **4**, 647–667.
- Iskenderian, H., J. R. Mecikalski, W. M. MacKenzie Jr., W. F. Feltz, and K. M. Bedka, 2009: Using satellite data to improve convective forecasts in the Collaborative Storm Prediction for Aviation (CoSPA). *Proc. First Atmospheric and Space Environments Conf.*, San Antonio, TX, AIAA.
- Johnson, R. A., and D. W. Wichern, 2002: *Applied Multivariate Statistical Analysis*. 5th ed. Prentice Hall, 730 pp.
- Kidder, S. Q., and T. H. Vonder Haar, 1995: *Satellite Meteorology: An Introduction*. Academic Press, 466 pp.
- Lensky, I. M., and D. Rosenfeld, 2008: Clouds-Aerosols-Precipitation Satellite Analysis Tool (CAPSAT). *Atmos. Chem. Phys.*, **8**, 6739–6753.
- Levizzani, V., and M. Setvák, 1996: Multispectral, high-resolution satellite observations of plumes on top of convective storms. *J. Atmos. Sci.*, **53**, 361–369.
- Li, X., S. Zhang, and D.-L. Zhang, 2006: Thermodynamic, cloud microphysics, and rainfall responses to initial moisture perturbations in the tropical deep convective regime. *J. Geophys. Res.*, **111**, D14207. doi:10.1029/2005JD006968.
- Lindsey, D. T., D. W. Hillger, L. Grasso, J. A. Knaff, and J. F. Dostalek, 2006: GOES climatology and analysis of thunderstorms with enhanced 3.9- μm reflectivity. *Mon. Wea. Rev.*, **134**, 2342–2353.
- Marr, D., and E. Hildreth, 1980: Theory of edge detection. *Proc. Roy. Meteor. Soc.*, **207B**, 215–217.
- Mecikalski, J. R., and K. M. Bedka, 2006: Forecasting convective initiation by monitoring the evolution of moving cumulus in daytime GOES imagery. *Mon. Wea. Rev.*, **134**, 49–78.
- , W. M. MacKenzie Jr., M. König, and S. Muller, 2010: Cloud-top properties of growing cumulus prior to convective initiation as measured by Meteosat Second Generation. Part I: Infrared fields. *J. Appl. Meteor. Climatol.*, **49**, 521–534.
- Nakajima, T., and M. D. King, 1990: Determination of the optical thickness and effective particle radius of clouds from reflected solar radiation measurements. Part I: Theory. *J. Atmos. Sci.*, **47**, 1878–1893.
- Purdom, J. F. W., 1976: Some uses of high resolution GOES imagery in the mesoscale forecasting of convection and its behavior. *Mon. Wea. Rev.*, **104**, 1474–1483.
- , 1982: Subjective interpretations of geostationary satellite data for nowcasting. *Nowcasting*, K. Browning, Ed., Academic Press, 149–166.
- Roberts, R. D., and S. Rutledge, 2003: Nowcasting storm initiation and growth using GOES-8 and WSR-88D data. *Wea. Forecasting*, **18**, 562–584.
- Rosenfeld, D., W. L. Woodley, A. Lerner, G. Kelman, and D. T. Lindsey, 2008: Satellite detection of severe convective storms by their retrieved vertical profiles of cloud particle effective radius and thermodynamic phase. *J. Geophys. Res.*, **113**, D04208. doi:10.1029/2007JD008600.
- Schmetz, J., P. Pili, S. Tjemkes, D. Just, J. Kerkmann, S. Rota, and A. Ratier, 2002: An introduction to Meteosat Second Generation (MSG). *Bull. Amer. Meteor. Soc.*, **83**, 977–992.
- Schmit, T. J., M. M. Gunshor, W. P. Menzel, J. J. Gurka, J. Li, and A. S. Bachmeier, 2005: Introduction to the next-generation Advanced Baseline Imager on GOES-R. *Bull. Amer. Meteor. Soc.*, **86**, 1079–1096.
- , J. Li, J. Li, W. F. Feltz, J. J. Gurka, M. D. Goldberg, and K. J. Schrab, 2008: The GOES-R Advanced Baseline Imager and the continuation of current sounder products. *J. Appl. Meteor. Climatol.*, **47**, 2696–2711.
- Scorer, R. S., 1986: *Cloud Investigation by Satellite*. Ellis Horwood, 314 pp.
- Setvák, M., and C. A. Doswell III, 1991: The AVHRR channel 3 cloud top reflectivity of convective storms. *Mon. Wea. Rev.*, **119**, 841–847.
- , R. M. Rabin, C. A. Doswell, and V. Levizzani, 2003: Satellite observations of convective storm top features in the 1.6 and 3.7/3.9 μm spectral bands. *Atmos. Res.*, **67–68C**, 589–605.
- Siewert, C. W., M. König, and J. R. Mecikalski, 2010: Application of Meteosat Second Generation data towards improving the nowcasting of convective initiation. *Meteor. Appl.*, **17**, 442–451.
- Weckwerth, T. M., and D. B. Parsons, 2006: A review of convection initiation and motivation for IHOP_2002. *Mon. Wea. Rev.*, **134**, 5–22.
- Weiss, C. E., and J. F. W. Purdom, 1974: The effect of early-morning cloudiness on squall-line activity. *Mon. Wea. Rev.*, **102**, 400–402.
- Wielicki, B. A., and R. M. Welch, 1986: Cumulus cloud properties derived using Landsat satellite data. *J. Climate Appl. Meteor.*, **25**, 261–276.
- Wilks, D. S., 2006: *Statistical Methods in the Atmospheric Sciences*. 2nd ed. Academic Press, 627 pp.
- Wilson, J. W., E. E. Ebert, T. R. Saxen, R. D. Roberts, C. K. Mueller, M. Sleigh, C. E. Pierce, and A. Seed, 2004: Sydney 2000 Forecast Demonstration Project: Convective storm nowcasting. *Wea. Forecasting*, **19**, 131–150.
- Wolfson, M. M., and D. A. Clark, 2006: Advanced aviation weather forecasts. *MIT Lincoln Lab. J.*, **16**, 31–58.
- Wulfmeyer, V., and Coauthors, 2008: The Convective and Orographically Induced Precipitation Study. *Bull. Amer. Meteor. Soc.*, **89**, 1477–1486.
- Zinner, T., H. Mannstein, and A. Tafferner, 2008: Cb-TRAM: Tracking and monitoring severe convection from onset over rapid development to mature phase using multi-channel Meteosat-8 SEVIRI data. *Meteor. Atmos. Phys.*, **101**, 191–210. doi:10.1007/s00703-008-0290-y.